Helvetica Physica Acta, Vol. 55 (1982) 100–121

0018–0238/82/010100–22$1.50 + 0.20/0

A high angular resolution 2-D correlation apparatus for positron annihilation studies

P. E. Bisson, P. Descouts, A. Dupanloup, A. A. Manuel,
E. Perreard, M. Peter and R. Sachot, Université de Genève,
Département de Physique de la matière condensée,
32 Bd d'Yvoy, CH-1211 Genève 4, Switzerland.

(22. III. 1982)

Abstract. We present an experimental system based on two high-density proportional chambers to detect the angular correlation of positron annihilation radiation (ACPAR) in solids. The main characteristic of this apparatus is its angular resolution of 0.24×0.3 mrad^2 which is four times better than other devices. A measurement in Nb is presented and a simple model is used to show that this apparatus gives a precise measurement of the valence electron momentum density.

Introduction

Positron annihilation is a method used for a long time to study the electronic properties of solids [1, 2]. In the last few years, the technological improvements of the 2-D γ-ray detectors have allowed a considerable progress in angular correlation measurements. The method is the following: positrons emitted from radioactive sources (^{64}Cu, ^{58}Co, ^{22}Na, . . .) annihilate with electrons of the sample. Two γ-rays are then emitted approximately in a straight line, but in opposite directions. The small angular deviation from 180° between the outgoing γ-rays is proportional to the component of the momentum of the electron–positron pair in the plane perpendicular to the direction of emission. Since positrons thermalize prior to annihilation, the measurement of these small angles (some milliradians) carries information closely related to the electron momentum distribution $\rho_e(\vec{p})$.

The difference between $\rho_e(\vec{p})$ and $\rho_{ep}(\vec{p})$, the electron–positron momentum density as determined with this method, is due to the following effects:

- electron–positron correlations that screen the positron moving in the electronic structure of the material disturb the local electron density around the positron,
- the overlapping of positron and electron wave functions which is not uniform: the positron is repelled from the core and moves mainly in the interstitial region.

The first effect is known to introduce small deviations $\varepsilon(\vec{p})$ from $\rho_e(\vec{p})$, which are moreover slowly varying with $\vec{p}$ [3]. The second has for consequence that positron annihilation is well suited to study valence electrons.

Finally, $\rho_{ep}(\vec{p})$ can be expressed as

$$\rho_{ep}(\vec{p}) = \varepsilon(\vec{p})\rho^{i}_{ep}(\vec{p}) \qquad (1)$$

where $\rho^i_{ep}(\vec{p})$ is the electron–positron momentum density in the approximation of independent particles. $\rho^i_{ep}(\vec{p})$ is closely related to $\rho_e(\vec{p})$ and can be evaluated from band structure calculation as

$$\rho^i_{ep}(\vec{p}) = \left| \sum_{\vec{k}_{occ}} \int d^3r \psi_k(\vec{r}) \psi_+(\vec{r}) e^{-i(\vec{p}\cdot\vec{r})} \right|^2 \tag{2}$$

where $\psi_k(\vec{r})$ is the electron wave function for the state $\vec{k}$ and $\psi_+(\vec{r})$ is the positron wave function (the positron being in the state $k=0$).

We show in this paper that the positron wave function does not induce large deviations, even in transition metals like Nb and, consequentely, that the measurement can be well understood on the basis of the simple approximation

$$\rho(\vec{p}) = \sum_{n,\vec{k},\vec{G}} n_n(\vec{k})\, \delta(\vec{p} - \vec{k} - \vec{G}) \tag{3}$$

where $n_n(\vec{k})$ is the occupation number of the state $\vec{k}$ of the valence electron in the Brillouin zone (BZ) and $\vec{G}$ a vector of the reciprocal lattice.

With 2-D γ-ray detectors, the measured quantity $N(\theta_x, \theta_y)$ is related to $\rho_{ep}(\vec{p})$ with

$$N(\theta_x, \theta_y) \div \int dp_z \rho_{ep}(\vec{p}) \tag{4}$$

where

$$\theta_\nu = \frac{p_\nu}{mc}, \qquad \nu = x \quad \text{or} \quad y$$

and z is the direction of propagation of the detected γ-rays.

Until now there have been three main designs for 2-D angular correlation measurements: multi-counter systems [4], Anger camera [5] and high-density proportional chambers [6].

This last technique is based on prototype detectors developed at CERN [7] and first used for positron annihilation in our institute [8]. In this paper we present a new experimental facility for which we have built larger and more efficient detectors. We illustrate its performance with a measurement in a Nb single crystal.

In the first section we describe the different parts of our system. In Section B, we describe its characteristics. The last section presents a measurement in Nb and its interpretation on the basis of a simple model for $\rho_{ep}(\vec{p})$.

Section A. Description of the System

1. *General description*

A schematic block diagram of our experimental set-up is shown in Fig. 1. It consists of a cryostat containing the positron source and the sample. It is positioned in the middle of a 22 m experimental area. On both sides of the cryostat lies a multi-stack high-density proportional chamber with a 400 cm^2 sensitive area. The detectors can be moved from 5 m up to 10.5 m apart from the

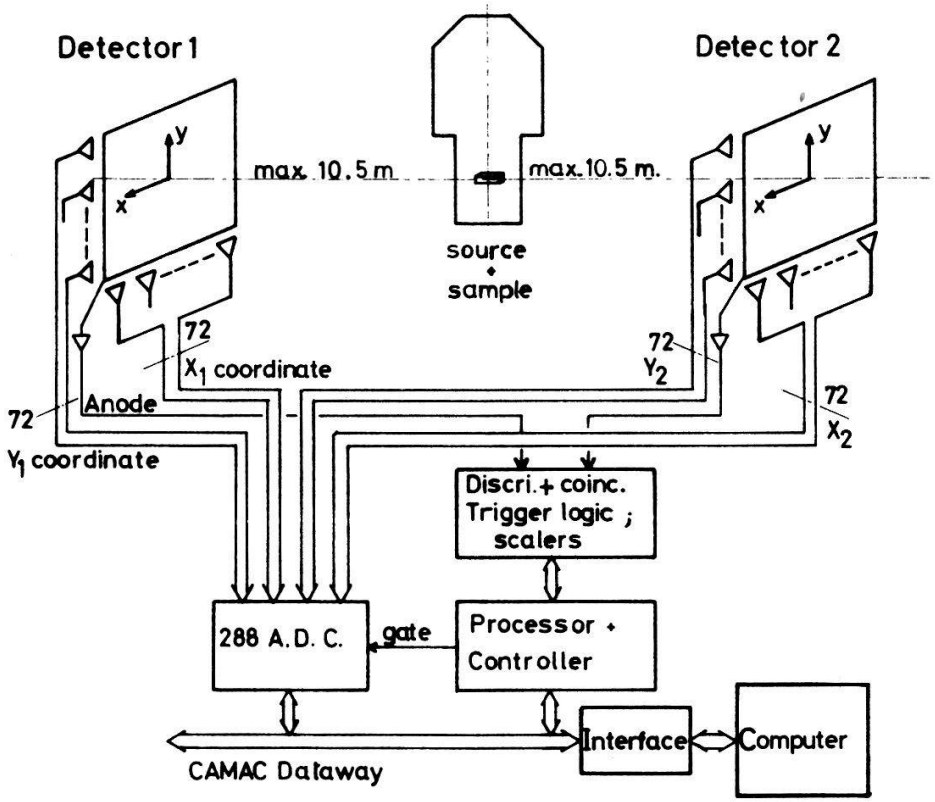

Figure 1.
General layout of the experimental system.

sample. They are connected to a read-out electronic composed of a coincidence trigger to detect the two γ-rays emitted simultaneously, and of a digital data acquisition system driven by a computer. The digital information is obtained via a set of analog-to-digital converters (ADC) connected to a front-end microprocessor. This information is used to calculate the two angle components (θ_x, θ_y) for each event from the positions (x_i, y_i) of the event in both detectors $(i = 1, 2)$

$$\theta_x = (x_1 + x_2)/L \tag{5.a}$$

$$\theta_y = (y_1 + y_2)/L \tag{5.b}$$

where L is the sample to detector distance.

2. *Cryogenic system and source–sample assembly*

For our experiment we have designed and built a cryogenic system satisfying several requirements for ACPAR measurements.

The special criteria imposed on the system are as follows:

- precise positioning of the sample relatively to the γ-ray detectors,
- focusing of positrons using a superconducting magnet,
- possibility of rotating the sample inside the cryostat to make measurements for different crystalline orientations,
- possibility of changing samples without radioactive source manipulation,
- sample-heater and temperature control to raise the sample temperature above 4.2 K,
- optical system to control the stability of the sample-holder during cooling,

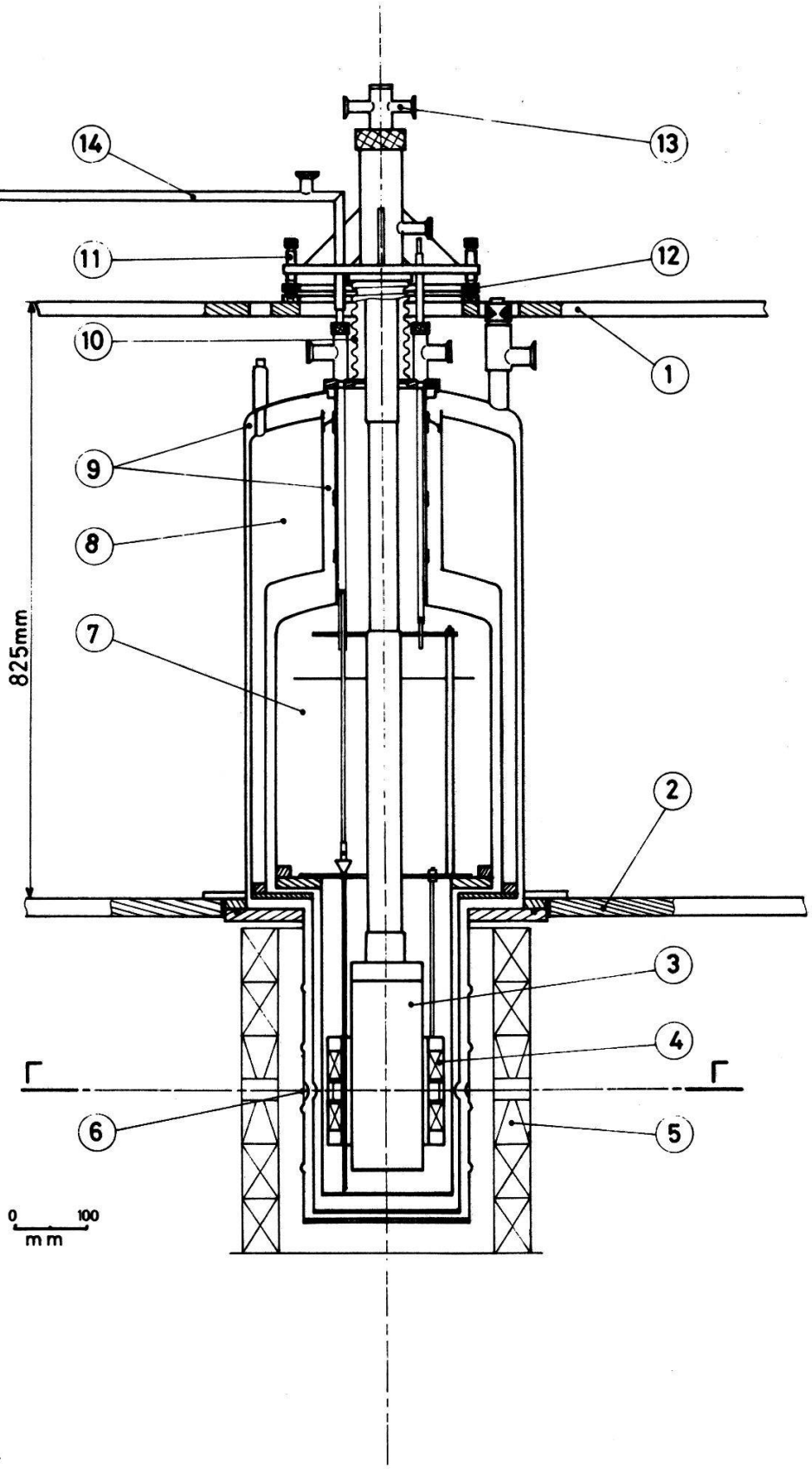

Figure 2.
Schematic vertical cross-section of the cryostat. The direction of the detected γ-rays is symbolized by the axis (Γ). {1}: support of the sample-holder; {2}: support of the cryostat; {3}: vacuum box holding the tungsten block, the ^{22}Na source and the sample; {4}: double coil superconducting magnet; {5}: lead bricks; {6}: titanium window; {7}: helium reservoir; {8}: nitrogen vessel; {9}: vacuum chamber; {10}: flexible tube; {11}: micro-screws; {12}: ball-bearings; {13}: sample-holder; {14}; helium filling pipe.

– a relatively low liquid helium consumption because precise measurements are long,

– special care must be taken to always have a clean sample and source chamber and to have the possibility to measure samples sensitive to oxidation,

– gamma irradiation shielding.

The structure of the cryogenic system is shown in Fig. 2. The tungsten block in which are placed the ^{22}Na source and the sample {3} is mounted on a support {1} independent of that of the cryostat {2}. These two parts are mechanically disconnected using a flexible tube {10}. Then we have the possibility to make a precise orientation of source and sample relative to the γ-ray detectors by mechanical adjustment {11, 12} using a theodolite. The body of our cryostat is from Thor Cryogenics, serie 700, with a 17.5 liters helium reservoir {7}. The nitrogen vessel has a capacity of 34 liters {8}. There is only one vacuum chamber {9}.

We have adapted tails on the cryostat for our experiment. Then we have the possibility of using a double coil superconducting magnet {4} to focus positrons on the sample. To minimize absorption of positrons and annihilation γ-rays, the ^{22}Na source and sample are in a vacuum box {3}. The walls of this box and of the inside tail of the cryostat are made of stainless steel and are as thin as possible to minimize absorption of annihilation γ-rays. In the intermediate copper tail there are two holes on the Γ-axis and on the outside tail two windows closed by thin titanium glued foils {6}. γ-rays from the source are screened by the tungsten block inside {3} and by lead bricks outside the tails of the cryostat {5}.

The sample–holder {13} has the possibility to rotate relative to the ^{22}Na source–holder around the vertical axis. A vacuum chamber is adjustable on the top of the cryostat when we have to introduce samples very sensitive to oxidation.

Liquid helium is filled through the tube {14} and we have two positions of filling at the bottom and on the top of the inside tail of the cryostat. When working at 4.2 K with the superconducting magnet the liquid helium consumption is around 0.4 l/h. Between two refills we have an autonomy greater than 48 hours and we have the possibility to refill without stopping measurements. Thus it is possible to make experiments continuously during several weeks if necessary.

The details of the construction around the sample are given in Fig. 3 which represents a cross-section of the system inside the box {3} of Fig. 2. We see the tungsten shield {1} on which the 52 mCi ^{22}Na source {2} is fixed and which is drilled with 4 mm diameter holes {3} on the Γ-axis. The source is positioned below the hole axis to prevent the detection of source γ-rays. The surface of the sample is on the Γ-axis and a few millimeters away from the source. The sample {4} is mounted on a goniometer head {5} for X-ray orientation outside the cryostat. A mirror {6} may be fixed to the bottom of the sample–holder tube to optically control the stability of the system when cooled down to 4.2 K. To work above 4.2 K, an electric heater {7} may be fixed on the neck of the sample–holder, and the temperature of the sample may be monitored by thermocouples.

The source–sample assembly is mounted in a vacuum chamber, then there is no absorption of positrons between the source and surface sample. γ-rays from the annihilation in the sample are partially absorbed by the walls of the chamber, by liquid helium, by the walls of the cryostat tails and by the air between the cryostat and the detectors. For a distance of 10.5 m between sample and detector the total absorption may be estimated at about 33% of annihilation γ-rays.

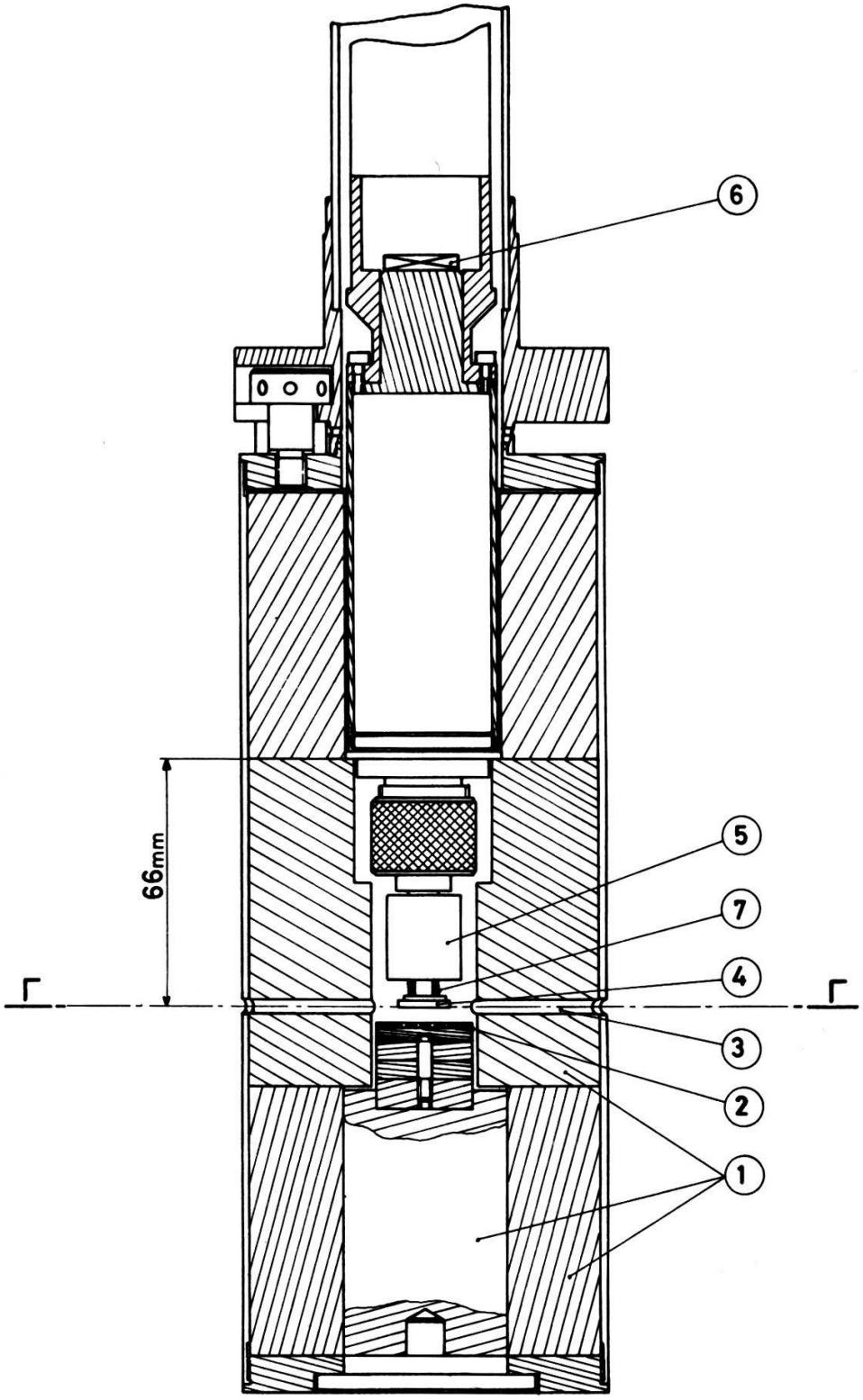

Figure 3.
Source-sample assembly. {1}: tungsten shield; {2}: ^{22}Na source; {3}: hole; {4}: sample; {5}: goniometer head; {6}: mirror; {7}: electric heater.

To focus the positron flux on the sample we use a superconducting magnet from Thor Cryogenics which gives a central field intensity of 2 Tesla. It is then possible to raise the counting rate by a factor 10 as can be seen in Fig. 4 which gives the coincidence rate versus magnetic field intensity for a sample with a $7.5 \times 1.5\,mm^2$ area surface illuminated by positrons and for a 5.9 mm source–sample distance.

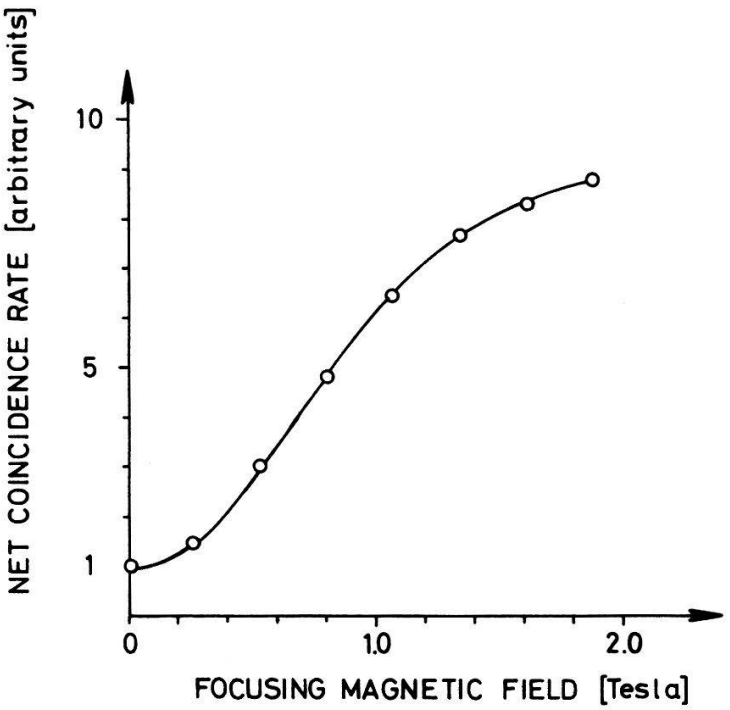

Figure 4.
Net coincidence rate vs magnetic field intensity (area of the sample: $7.5 \times 1.5\ mm^2$, source-sample distance: 5.9 mm, distance between detectors: 21 m, T = 4.2 K, source: 52 mCi ^{22}Na).

3. *Detectors*

It is well known that for the study of the ACPAR a good angular resolution is necessary. For a given and reasonable sample to detector separation, we choose the detector which has the best spatial resolution. This is achieved by the high-density proportional chamber (HDPC) [9]. Despite its relatively low detection efficiency compared with other types of detectors [4, 5], the HDPC has a very good spatial resolution and a continuous detection in both directions (x and y). It is then not necessary to move the detectors during the data acquisition.

(a) *Principle of operation.* A multiwire proportional chamber (MWPC) has a very poor detection efficiency for a 511 keV γ-radiation. It is thus necessary to convert the radiation into an ionizing particle to perform an efficient detection. This is achieved with a stack of high-density conducting sheets interleaved with insulating foils (Fig. 5). The whole stack is drilled of holes. Each conducting sheet is at an increasing potential, so creating an electric field parallel to the hole axis.

The photo- or Compton-electron produced by a gamma interaction in the material has a non-negligible probability to escape in a hole and to ionize the gas flowing in the detector. Under the electric field effect the secondary electrons drift in the MWPC for further detection.

The MWPC consists of three planes of wires: a thin wire plane (anode) between two crossed cathode wire planes (Fig. 5). Due to the very high radial electric field around the anode wires, the drifted electrons are accelerated and ionize the gas. An avalanche is produced and the initial charge is amplified. The produced ions are rapidly pushed back to the anode wire, inducing positive pulses on the surrounding electrodes. A calculation of the centers of gravity of the induced pulse distributions on the orthogonal cathode wire planes readily gives the two coordinates of the impinging γ-ray [10].

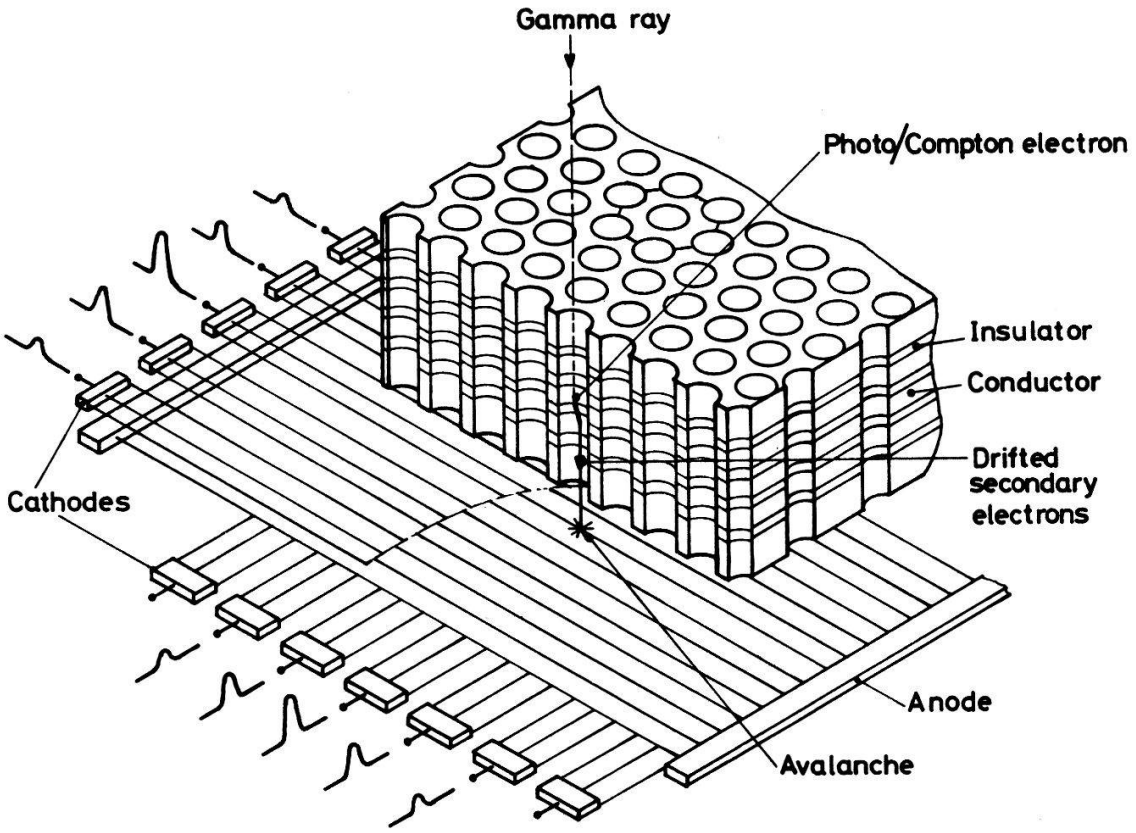

Figure 5.
Gamma to electron converter and multiwire proportional chamber.

(b) *Multiwire proportional chamber.* As observed in our prototype detectors [8] problems arise when an event occurs near the edges of the MWPC, because for this event the calculated center of gravity of the induced pulses on the cathode is displaced towards the center of the chamber. In order to suppress this effect we have built the wire planes greater than the sensitive area of the converters.

We have also added guard strips between the wire planes.

The anode plane consists of 216 gold-plated tungsten wires of 20 μm in diameter spaced at 1 mm. The cathode planes are made of 216 bronze-beryllium wires of 100 μm in diameter spaced at 1 mm. The cathode–anode distance is 3 mm. When the gas inside the MWPC is isobutane the applied high voltage on the anode is 5 kV, the cathodes being at ground potential.

All anode wires are connected together. Three contiguous cathode wires are connected together to form a read-out channel [11].

(c) *Converter.* The manufacturing process of a converter is the following: a stack of eight 0.2 mm thick sheets of a lead–antimony alloy interleaved with 0.1 mm thick sheets of Teflon glued together with epoxy resin is drilled over a 20×20 cm^2 area according to an hexagonal pattern using a numerically controlled printed circuit drilling machine. A chemical treatment removes the possible short-circuits between conductor pairs. Four such stacks aligned with a binocular and firmly maintained together forms a 1 cm thick converter.

In order to compare converter efficiencies we have built and tested two types of converters. The first with 0.6 mm diameter holes on 0.8 mm pitch, the second with 0.8 mm holes on 1 mm pitch. The optimum wall thickness between holes

being 75 μm for 0.5 MeV photons [12] the ratio of the areas where the photo-electron can escape in a hole for the two different patterns is 1.17, i.e. a more favourable detection efficiency for the 0.6 mm diameter hole geometry. On the other hand the range of the photo-electron is in mean shorter in a 0.6 mm diameter hole, leading to a smaller quantity of secondary electrons. Another parameter to take into account is the inside hole area where the electric field lines are continuous [12]; this parameter is strongly influenced by the stack regularity and the absence of short circuits. The efficiency is about 7% better for converters with 0.6 mm diameter holes compared with the 0.8 mm ones.

In order to minimize the electron losses during drift, we have slightly focused the electric field in the direction of the drift. So the electric field in the converter varies from 1 kV/cm to 2 kV/cm.

The photo- or Compton-electron escaping in a hole can take any direction. Its range has any length, leading to a variable quantity of secondary electrons. Due to this effect our detectors have no energy resolution.

(d) *Detector assembly.* Each detector can be divided in two identical parts (Fig. 6). Each part consists of a MWPC sandwiched between two converters. The electric fields in the two converters are in opposite directions, so we need only one MWPC to collect the drifted secondary electrons from two converters. The holes

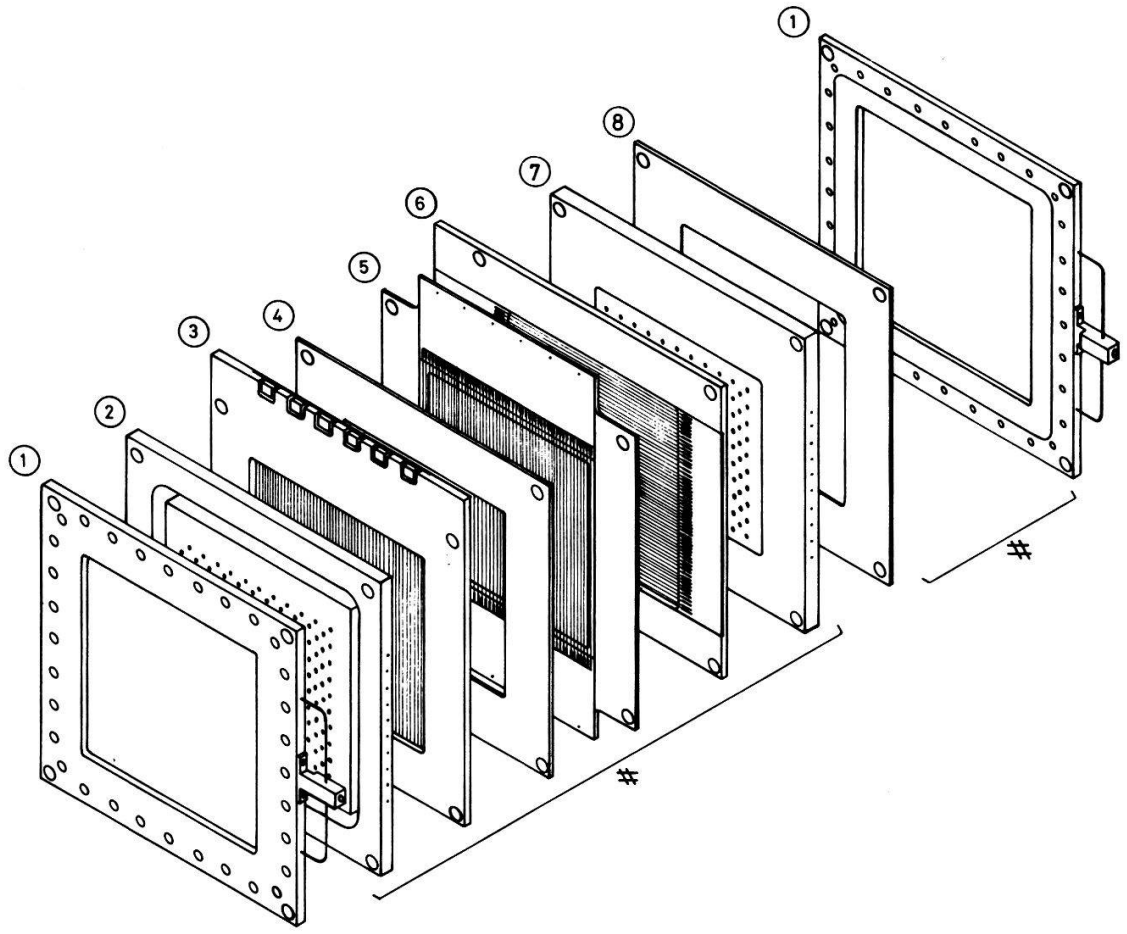

Figure 6.
Converters and wire planes layout in a detector; {1}: window frames; {2}, {7}: gamma to electron converters; {3}, {6}: cathode wire-planes; {4}, {8}: spacer frames; {5}: anode wire plane.

of the converters are offset to increase the interaction probability of the γ-rays. Both the 0.6 mm diameter holes converters lie at the photon source side.

The read-out channels of each cathode plane pair with the same wire direction in the detector are connected in parallel, so we have one and only one x and y coordinate per detector.

(e) *Gas.* The ideal gas should have the following properties: a high specific ionisation for fast electrons, high charge amplification during the avalanche process, multi-energy levels in the UV region for stable operation and high electron drift velocity to minimize the coincidence resolving time. Pure isobutane (C_4H_{10}) offers a good compromise between these requirements. Although most gases have a sufficient charge amplification, other gases, such as methane, have a high saturated drift velocity (10 cm/μs), but are relatively transparent for electrons of few hundreds keV. In the case of isobutane we can easily reach an amplification of 10^4–10^5 and a specific ionisation of about 250 electrons/cm, with an electron saturated drift velocity of 5 cm/μs. The drift velocity and the thickness of the converters determine the resolving time of our detectors which is 300 ns in our case.

4. *Electronic hardware and data acquisition*

(a) *Electronic hardware.* Each read-out channel is connected to a charge-sensitive amplifier (Fig. 7) followed by a variable gain amplifier and a 50Ω cable driver. Such amplifier adapted to our requirements is not available commercially so we have designed and built low cost amplifiers grouped by twelve on a printed circuit board. Special attention has been taken to prevent diaphony between channels (>40 dB). This amplifier is a simplified version of the one described in

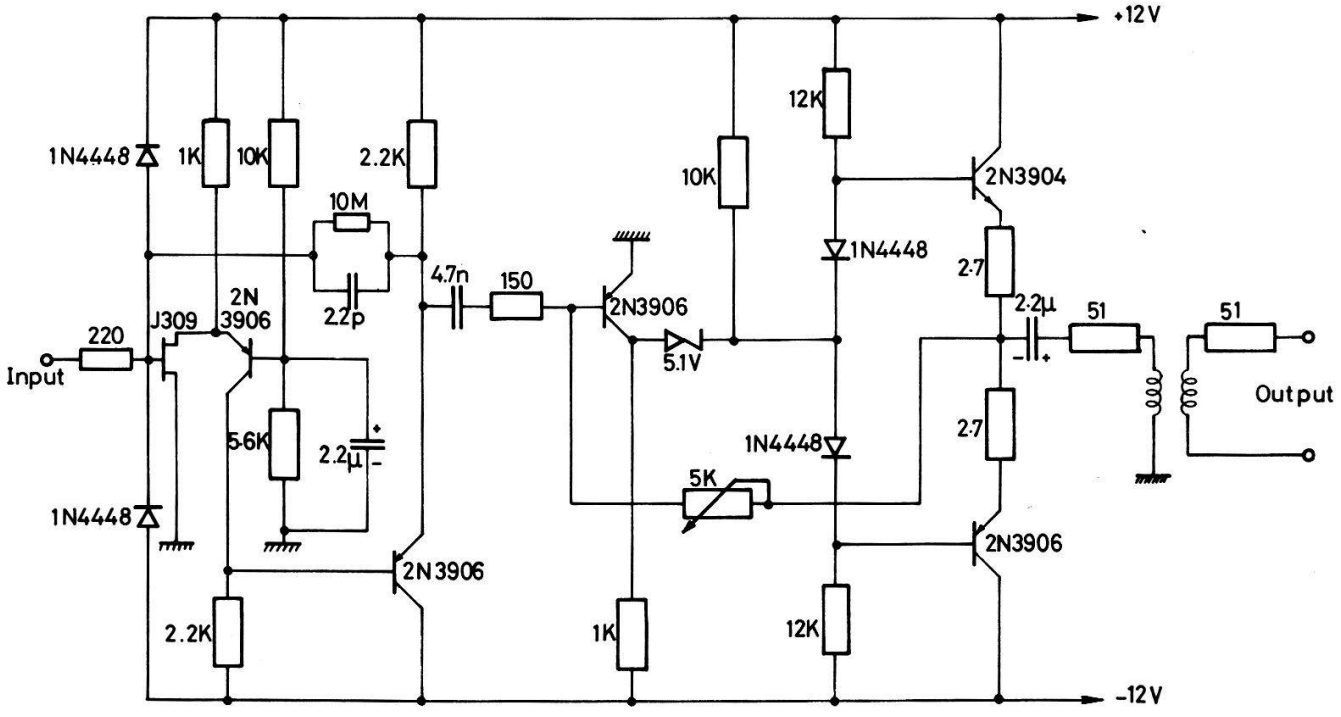

Figure 7.
Charge-sensitive amplifier for cathode read-out.

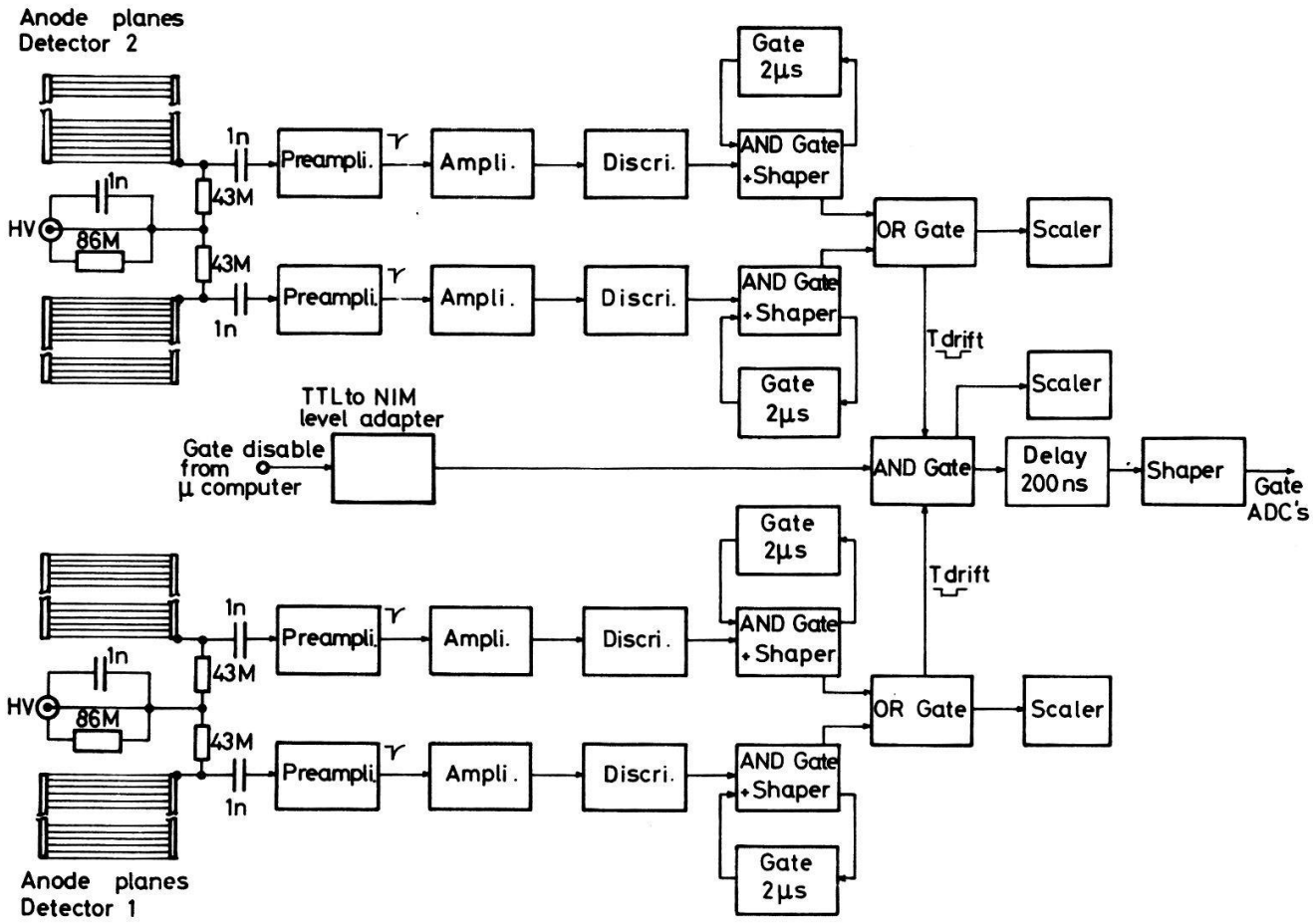

Figure 8.
Trigger logic of 2-D ACPAR.

[13]. These characteristics are: overall sensitivity 1 V/pCb; noise (peak to peak) $< 10^{-3}$ pCb; rise-time 30 ns; linearity $\simeq 1\%$. The outgoing signals are sent into a 10 bits ADC.

The four amplified signals from the anode planes are used in the trigger logic (Fig. 8). The amplified and shaped signals from the two anode planes of each detector are sent in a OR gate. Then the resulting signals are put in coincidence to provide the gate signal for the ADC. Taking into account the overall amplification and the discriminator threshold one electron is detectable and can contribute to the coincidence signal. A CAMAC crate holds all the ADC and a cabled microprocessor (LeCroy system).

(b) *Digital processing.* Figure 9 shows the data flow across the digital read-out, from the detectors upto the 2-D angular histogram.

For each event 288 values are collected by the microprocessor LeCroy 2280. Each value is proportional to the charge induced on the corresponding read-out channel. The value is different from zero in the neighbourhood of the avalanche. The microprocessor performs a preliminary data reduction on the basis of a minimum significant value for a digitalized pulse and sends an interrupt to the computer (VAX-11/780).

A device driver specially developped for the ORTEC DC011 CAMAC interface is entered. It adds the block of compressed data to a so-called 'system

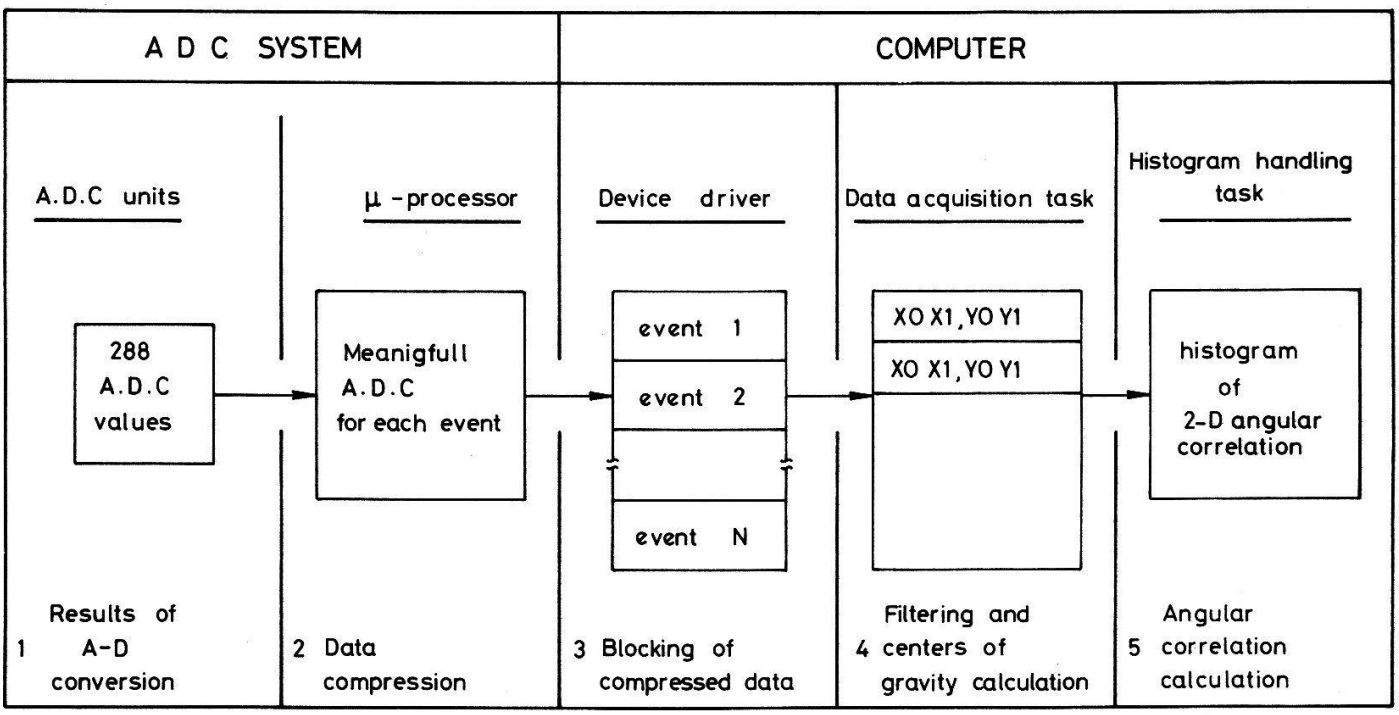

Figure 9.
Data flow in the acquisition system.

buffer' which is included, as well as the driver, in the operating system of the computer. This procedure has been adopted because it minimizes the CPU time used to perform this input operation. When a given number (usually 50) of blocks have been concatenated in the system buffer, they are sent to the data acquisition task, a FORTRAN program controlling all the procedures described in this paragraph. This task checks each block in the system buffer to decide if the corresponding event has to be rejected. This filtering procedure is based on the following criteria:

- none ADC is overload,
- one cluster of pulses and only one is found on each of the 4 read-out planes (x and y for two detectors),
- the extent of each cluster is between 2 fixed limits (2 and 10 read-out channels),
- the sum of the data in each cluster is between 100 and 4000; the first value is about 3 times the discrimination level used in the front-end microprocessor to define valid data; the second value corresponds to 4 pulses giving the full scale count.

The filtering procedure rejects $40 \pm 5\%$ of the collected events. For those accepted the data acquisition task calculates the coordinates (x, y) in the 2 detectors and adds these 4 values to a buffer contained in a so-called 'global section'.

The global section can be read by any task connected to it. One of these tasks builds the 2-D angular correlation histogram. Other tasks, not shown in Fig. 9, are used to control the detectors, either to produce on line visualisation of the detected γ-rays or to increment the histograms giving, for example, the response of the detectors as a function of the position or to retrieve information about the gain of the amplifiers, the integrity of the ADC and so on.

The data flow described here in a synchronous way is in fact an asynchronous process. Both the system buffer and the global section are multiple buffering structures. In this way, it is possible to establish a hierarchy of priorities which garantees a non-interrupted read-out of the detectors together with a flexible procedure suitable to the conditions imposed by the other users of the computer.

The whole data acquisition uses about 20% of the CPU time. 5% of which run in a high priority processor mode. the memory needed to run the system is 40 kbytes, without the 2-D angular correlation histogram calculation. Other 160 kbytes are used to contain the most often referenced parts of the histogram.

Section B. Characteristic properties of the experimental system

1. *Spatial resolution*

The number of secondary electrons reaching the anode wires varies from one or two up to some hundreds. For a given gas amplification and a large number of secondary electrons it is possible to reach the saturation of the amplification in the gas ($\approx 10^6$ electrons in the avalanche). In this case the spatial resolution in the x direction is given by the anode spacing. This is a 1 mm width square function. However it has been shown [14] that for an amplified charge before

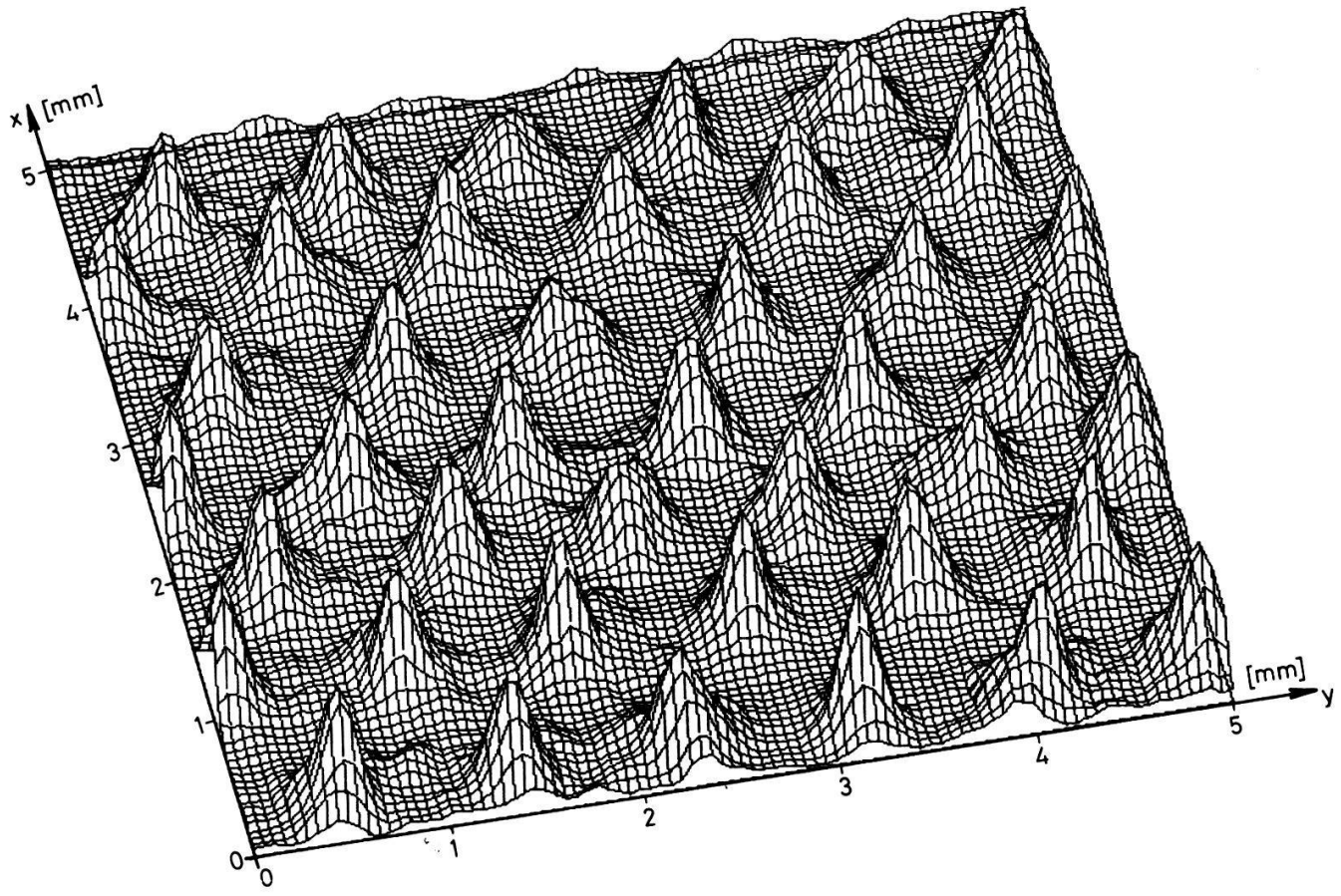

Figure 10.
2-D distribution of calculated position for events striking a $5 \times 5\ mm^2$ area of the converter {2} (0.6 mm diameter holes on 0.8 mm pitch). Each peak represents a hole. The hexagonal pattern of holes is clearly visible.

saturation, an interpolation between wires is possible with the centre of gravity read-out method. In the parallel direction of the anode wires (y) the spatial resolution is homogeneous for the interacting photons in the converter {2} (Fig. 6). On the other hand for interacting photons in the converter {7} the spatial distribution is modulated by the cathode wires due to their shadow effect on the secondary drifted electron [6].

We have recorded a 2-D histogram (Fig. 10) of the centre of gravity distribution for events in the converter {2} (0.6 mm diameter holes on 0.8 mm pitch). The histogram is an image of a $5 \times 5\,mm^2$ area of the detector surface. Each peak represents the calculated position in the MWPC of the drifted secondary electrons issued from a given hole in the converter. The distance between peaks is the hole pitch. All the peaks are well separated and the hexagonal pattern of holes is clearly visible. We deduce that the resolution of our read-out is 50 μm.

The spatial resolution of the whole detector is only restricted by the geometry of the hole pattern in the converters and by the wire plane arrangement. The spatial resolution is then 0.9 mm (1 mm) in the x (y) direction respectively.

2. *Angular resolution*

The angular resolution is the crucial parameter for the study of electronic properties using ACPAR. The reason is that the magnitude of the BZ corresponds to some milliradians, one order of magnitude above the resolution.

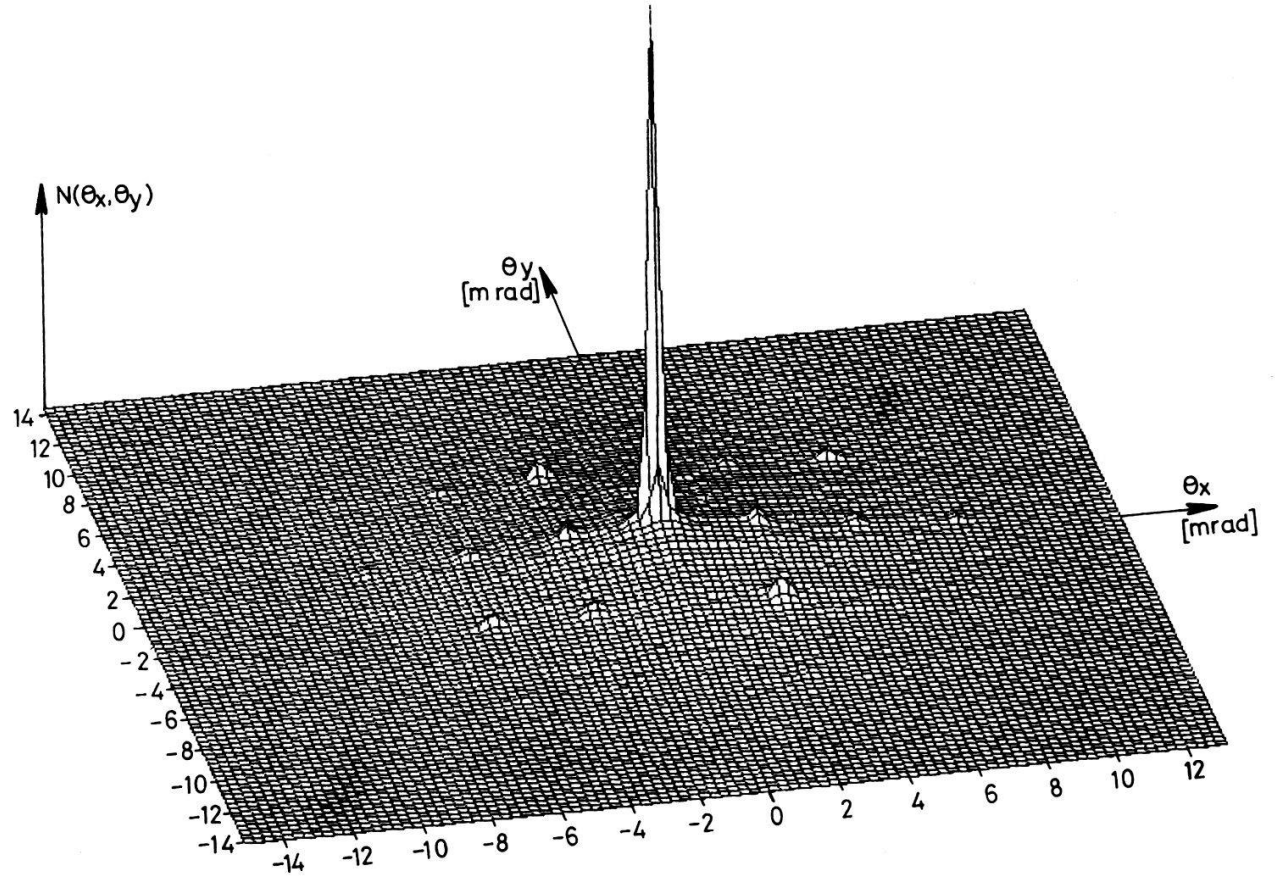

Figure 11.
Positronium annihilation peak measured in a single crystal of quartz at 4.2 K. The network used in this graphic is of 0.286 mrad.

Consequentely, an increased angular resolution is mandatory in many cases and can be the key to resolve the fine structures of the Fermi surface. Up to now, the best angular resolution for a 2-D machine was 0.7×0.7 mrad^2 [5, 6].

We have determined the angular resolution of our apparatus by measuring the positronium peak in crystalline quartz. The measurement was performed at the temperatures of 300 K, 77 K and 4.2 K. The results for this last temperature are shown in Fig. 11.

Assuming that the positron is thermalized in this sample at this temperature and that the intrinsic width of the positronium peak is negligible at this scale, we can attribute the width of the peak to the finite resolution of our experimental set-up.

In the direction parallel to the positron beam (y axis) the penetration of positrons into the sample has a negligible influence on the angular resolution, thus leaving the contribution of the detectors as the critical factor. Figure 12 shows the data points for small θ_y at $\theta_x = 0$. From this figure, we deduce the full width at half maximum of 0.24 mrad for the resolution. In the direction perpendicular to the positron beam (x axis), the observed fwhm is 0.3 mrad, for a 1.2 mm width sample. It is interesting to compare this value with the value of 0.5 mrad obtained with a sample of 5 mm width when using focusing magnetic field. It shows that the beam of positrons emitted from the 1.1 ± 0.1 mm width source is 2.0 mm wide when it reaches the sample.

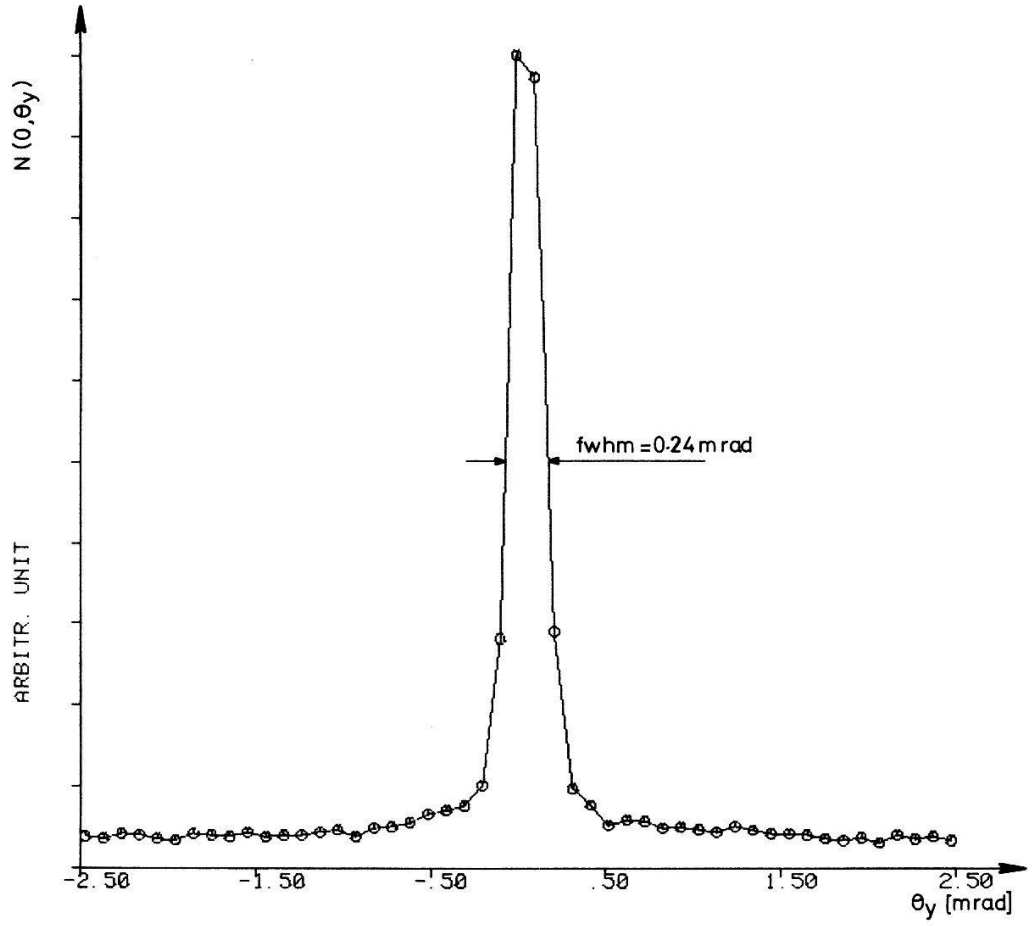

Figure 12.
The line $N(0, \theta_y)$ extracted from the 2-D distribution shown in Fig. 11. The data points, spaced at 0.103 mrad, are joined by straight lines. Error bars are less than the size of the points.

To conclude, it is better to use thin samples, with a length at least equal to the length of the source (10 mm in our case). With this geometry the greatest resolution ($0.24 \times 0.3\,\text{mrad}^2$) is obtained but a sample can be used to investigate only one plane in the electron–positron momentum distribution $\rho_{ep}(\vec{p})$. Nevertheless, it is possible to use disk shaped samples without degrading the 0.24 mrad resolution in θ_y, but with a resolution of 0.5 mrad in θ_x. In this case, one sample can be used to investigate many planes in $\rho_{ep}(\vec{p})$ when rotated around the disk axis.

3. *Detector efficiency, counting rate and signal to noise ratio*

The detector efficiency is difficult to measure. We tried to measure it by putting a ^{22}Na source between the detector under test and a NaI detector followed by a constant fraction discriminator with an energy window set on the 511 keV photopeak. The result is $6.5 \pm 0.5\%$ for a 1 cm thick converter with 0.6 mm diameter holes and the overall efficiency of each detector is $16 \pm 1\%$.

The counting rate depends on many geometrical parameters as well as of the sample. The counting rate is 150 events/s if measured in the following experimental conditions:

- distance between the two detectors: 21 m (resolution $0.24 \times 0.3\,\text{mrad}^2$)
- sample: single crystal of SiO_2, $1.2 \times 14\,\text{mm}^2$ in area placed at 6 mm from a shielded 52 mCi ^{22}Na source
- sample and source in vacuum at liquid helium temperature
- magnetic field: 2 Tesla
- flowing gas in the detector: isobutane
- resolving time: 300 ns

The signal to noise ratio (S/N) is estimated from the accidental coincident event rate. In acquisition the S/N ratio is a complicated pile-up of stochastic processes. We have compared the S/N ratio during and after acquisition. No great difference appeared because the acquisition time for an event is short (1.4 ms). The S/N ratio varies from 11 to 23 for detector–detector distances from 10 m to 21 m.

Section C. Results on niobium

The ACPAR in Nb has already been measured using a conventional long slit (one dimensional) apparatus [15] and compared with results based on APW band structure calculation [16]. These two studies conclude that the measurement can only be understood on the basis of a complete calculation including both electron and positron wave functions in the independent particles approximation:

$$N(p_z) \div \int dp_x\, dp_y \rho^i_{ep}(\vec{p}) \tag{6}$$

In this expression $N(p_z)$ is the angular correlation curve obtained with the conventional 1-D measurement and $\rho^i_{ep}(\vec{p})$ the expression defined in equation (2).

The first 2-D angular correlation measurements in Nb [17, 18] were both performed with a resolution of $0.7 \times 0.7\,\text{mrad}^2$. In this section we present the results of new measurements, with the current resolution of $0.24 \times 0.3\,\text{mrad}^2$ and

we show that the Fermi surface topology can be well understood on the basis of a simple calculation based on the cross-section of the Fermi surface as obtained with the LMTO method [21].

1. *Measurement*

The sample is a single crystal 5N purity carefully annealed. The surface exposed to positrons is $12 \times 1.2\,\text{mm}^2$, the thickness of the sample is 2.5 mm. It has been spark machined into a cylinder furnished by P. Bujard [19]. Its surface is 1° inclined from the crystallographic direction in order to avoid deviations due to the absorption of γ-rays in the sample itself. After annealing for 24 hours at 1000°C, it was fixed on the goniometer of the sample-holder and carefully aligned using X-rays to have the [110] direction along θ_y and [001] along θ_x.

The data acquisition was performed with the two detectors at 10.5 m from the sample. The focusing field was 1.5 Tesla for this run. The temperature of the sample was $5 \pm 1\,\text{K}$ during the 12 days of nearly continuous measurement. 4.7×10^7 events were recorded to build a 2-D angular distribution histogram of 400×400 bins covering an angular range of 41.2 mrad in both direction. The raw counting rate was 85 cps for the angular resolution of $0.24 \times 0.3\,\text{mrad}^2$.

The angular efficiency function was determined just after the measurement. It consists of taking data with an anticoincidence trigger, all remaining parameters being unchanged [20] and to build an histogram with 5×10^8 counts. This last operation can be performed off line using a relatively limited set of prerecorded events on each detector, so 2 hours are sufficient to effectively perform this calibration measurement.

The raw 2-D angular correlation histogram is divided bin per bin by the angular efficiency histogram normalised to unity at the peak. The resulting histogram contains 4500 counts at the top. The technique of redundant histograms [20] is used to build an histogram with the same bin size but where

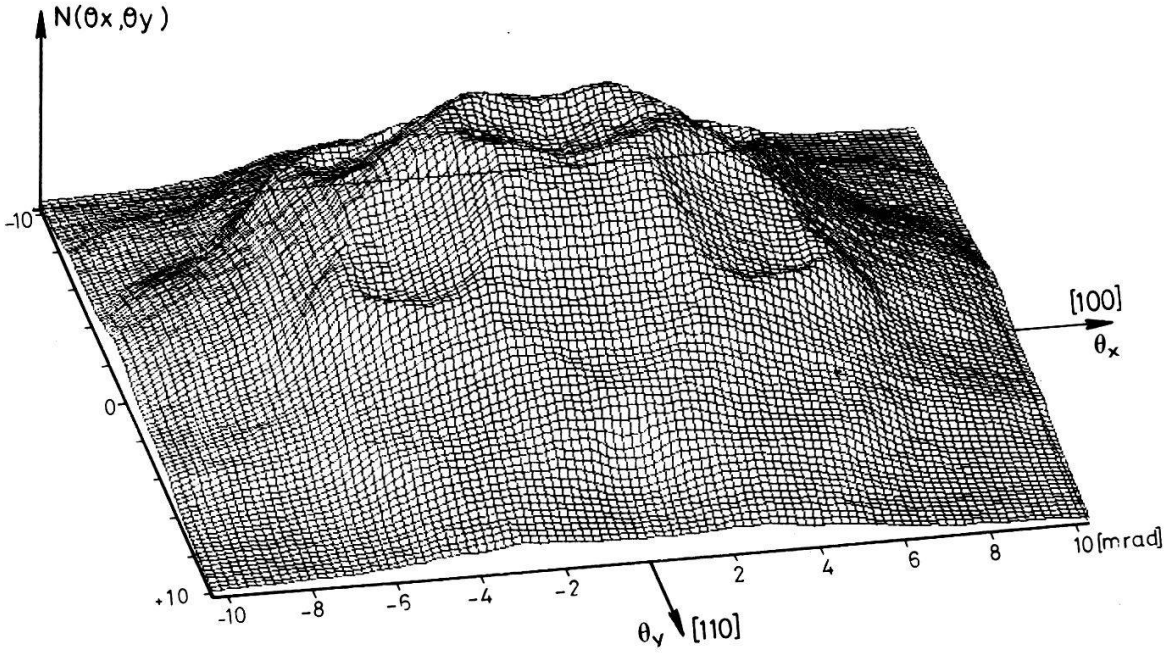

Figure 13.
2-D angular correlation obtained in the $(01\bar{1})$ plane for Nb with an angular resolution of $0.24 \times 0.3\,\text{mrad}^2$.

independent data are spaced by 0.3 mrad in both direction. By this way the top is 4×10^4 and no smoothing is applied to the data. The result is shown in Fig. 13 where one line is drawn each two rows and two columns, for clarity. So much information is contained in this measurement that it is difficult to draw all the angular range. In fact the large number of data points is mainly useful during data analysis.

The increased resolution of this measurement reflects itself in the recorded structures which are more pronounced than in the previous 2-D measurements [17, 18]. Thus it is evident that the study of electronic structure properties take advantage of the high angular resolution of our apparatus. This advantage would be more crucial in systems where the BZ is smaller than the present one ($\overline{\Gamma H}$ is 7.48 mrad for Nb).

2. *Analysis*

We have performed the p- to k-space reduction using the folding procedure known as the Lock–Crisp–West (LCW) theorem [22]. It is well known that the main characteristics of this procedure are, in the case of the independent particle

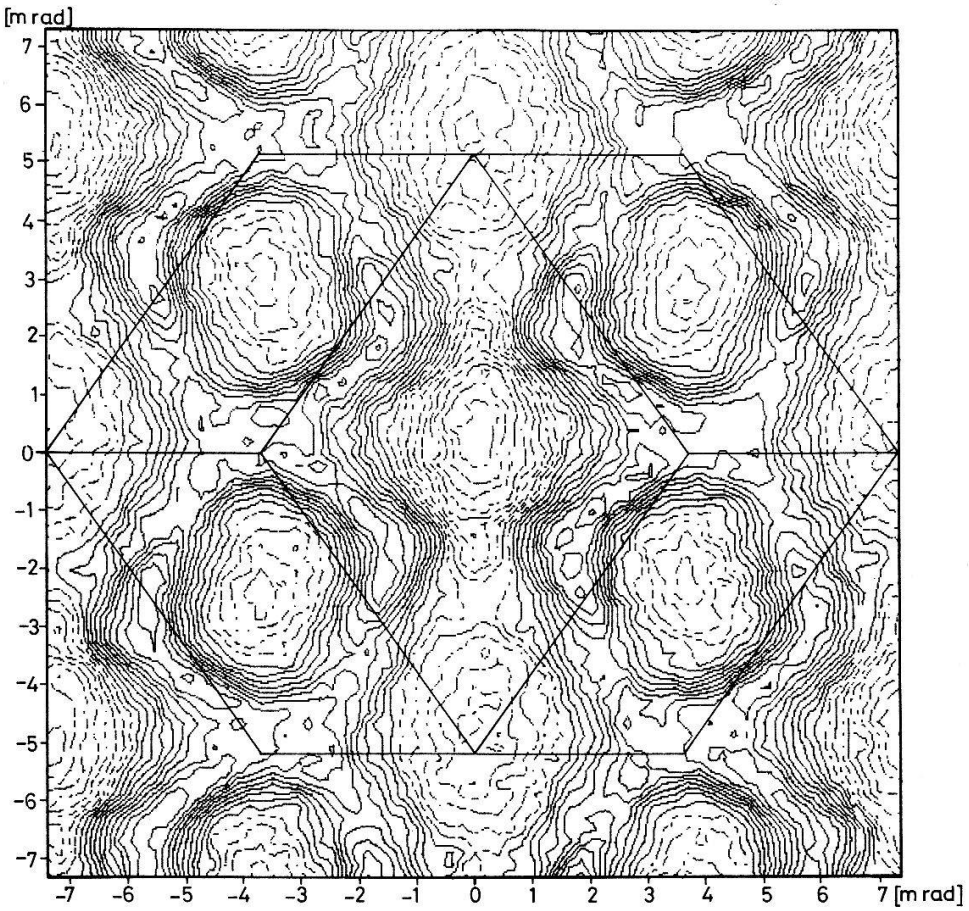

Figure 14.
2-D angular correlation of Nb reduced to k-space. The lines show the projection of the BZ in the [01$\bar{1}$] direction. The dashed contour lines lie in the lower part of the distribution. Distance between contour lines is 5% of the total anisotropy.

model and when the positron wave function $\psi_+(\vec{r})$ is constant:

- the contribution of filled bands to the integrated momentum distribution is constant in the plane of the BZ perpendicular to the z direction where our measurement is an integration of ρ_{ep} (see equation 4).
- the resulting distribution is independent of the particular shape of the electron wave functions.

Usually the independent particle model is a relatively good approximation and deviations due to the breakdown of this model are smooth distributions, the enhancement factors [3], and one can assume that no structure is added, suppressed or even shifted as a result of the correlations between electrons and positrons.

The effect of the positron wave function $\psi_+(\vec{r})$ can be more important to distort the angular distribution reduced to the k-space from a chart of the occupied states. $\psi_+(\vec{r})$ has been calculated for Nb [16] and the result shows that the radial part of $\psi_+(\vec{r})$ is a slowly varying function particularly in the interstitial region where its overlapping with the electron wave functions is significant. The positron remaining at the bottom of its band (s-state), no node of the angular part of $\psi_+(\vec{r})$ may induce major distortion. We can conclude here again that the LCW analysis in Nb is helpful to show the Fermi surface topology from the measured 2-D angular correlation.

The result of this analysis performed without either interpolation or smoothing is presented in Fig. 14. The 19 contour lines are equally spaced between 0.05 and 0.95 of the total anisotropy which represents 24% of the total amplitude

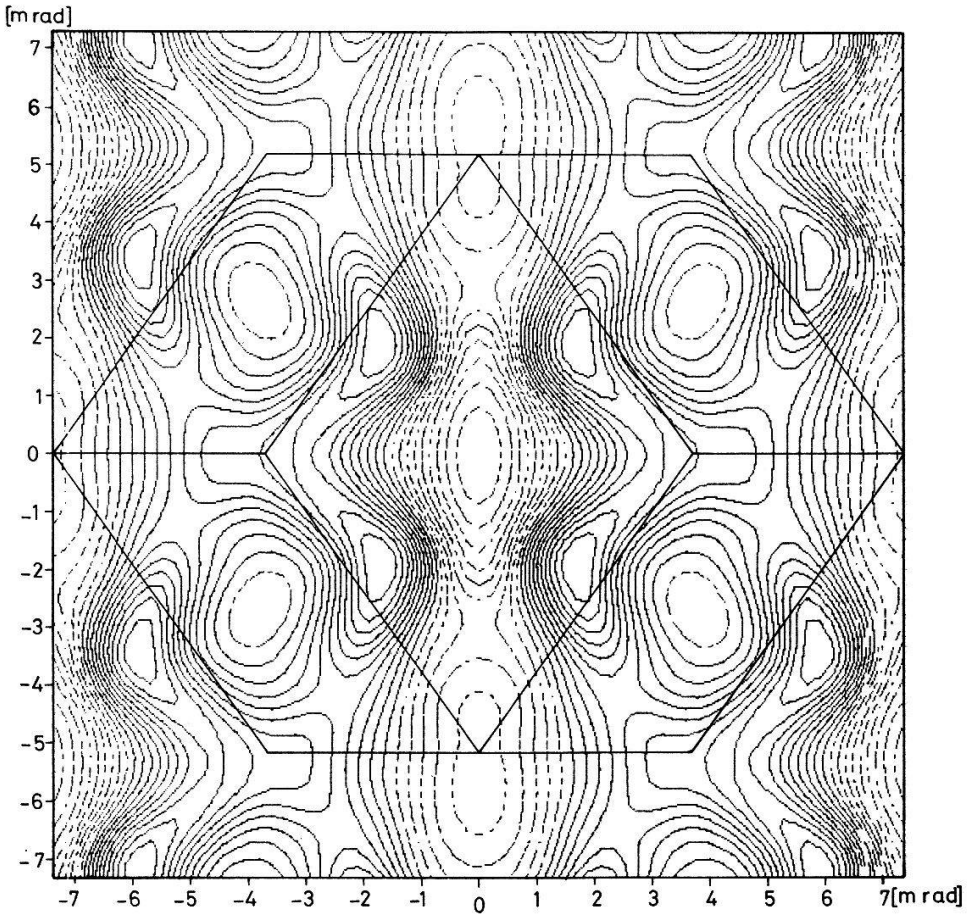

Figure 15.
The calculated distribution corresponding to Fig. 14.

of this distribution. Deeps are observed at the Γ point (center of the zone) and at the projection of the N point (center of the lozenges), as expected from the known Fermi surface. A simple calculation of this distribution has been done on the basis of the simple formula

$$N(p_x, p_y) \div \int dp_z \rho(\vec{p}) \tag{7}$$

This formula differs from (6) in the following ways:
- only one integration is done because we have now 2-D angular correlation,
- The approximate expression (3) is used for the momentum distribution.

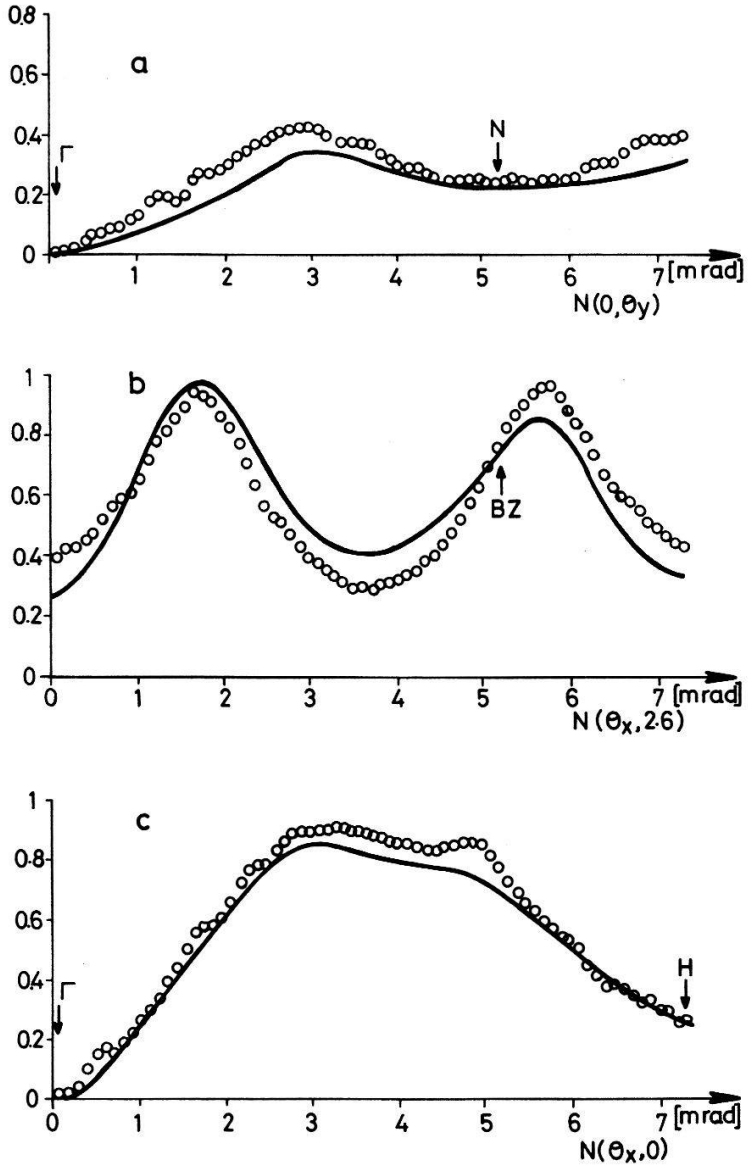

Figure 16.
Comparison of the experiment (points) with the calculated distribution (lines) along three paths in the $(01\bar{1})$ plane of the BZ. (a) the line $\overline{\Gamma N}$: $N(0, \theta_y)$; (b) a line parallel to $\overline{\Gamma H}$, but at intermediate distance between Γ and N; (c) the line $\overline{\Gamma H}$: $N(\theta_x, 0)$. The vertical scale is normalized to the maximum anisotropy.

For this calculation $n_n(\vec{k})$ of equation (3) has been obtained from a band structure calculation [21] solved self-consistently using the LMTO method for 7 bands near to the Fermi energy. The mesh of the calculation is 24 points along the $\overline{\Gamma H}$ line, it has been interpolated to give a mesh 3 times smaller. Once $N(k_x, k_y)$ has been calculated using equation 7, a convolution is performed with a bidimensional Gaussian to take into account the finite angular resolution of our set-up.

The result is shown in Fig. 15 for the same contour lines as in Fig. 14. It is evident that our simple model reproduces all the features of the experimental distribution. This demonstrates that positron annihilation can produce charts of the occupied states not only in simple metals but in the transition metals too, despite their complicated Fermi surface topology.

A quantitative comparison of the measurements with the model distribution described above is shown in Fig. 16 for three particular lines. Because we do not know how to separate the contributions of the core from the conduction electrons, the normalisation has been chosen as follow: a constant background has been substracted and the full anisotropy has been normalised to unity. Figure 16 demonstrates that these two approximations used for the calculation of the model distribution do not change the structures themselves but only affect their amplitudes. A more precise calculation (including electron and positron wave functions) is now in progress.

Conclusion

The main progress we have obtained with our new apparatus is a very good angular resolution, $0.24 \times 0.30\,\text{mrad}^2$ for a distance of 21 m between detectors and with a resonable counting rate, 150 cps/s. For the studies where such a good resolution is not necessary we can work with a detector to detector distance of 10 m and thus increase the counting rate by a factor of 4.

The excellent resolution of our system gives us the possibility to make precise measurements of the valence electron momentum densities of transition metals and compounds with small BZ. A complicated Fermi surface is no longer an obstacle to obtain good charts of the occupied states as we have demonstrated for Nb metal and we are now ready to work on more complicated or new compounds and to study small anisotropy effects due to many-body interactions.

Acknowledgements

To develop our new system we have greatly profited of the know-how gained during the construction of the prototype in collaboration with Dr. A. P. Jeavon's group at CERN. We benefit of the technical assistance of the services of our department, of the Nuclear Physics department and of the general services of the Institute of Physics.

To solve some technological problems, such as leakage from the cryostat or precise alignment of our experimental set-up we have benefited from the technical assistance of CERN.

The SiO_2 sample was given to us by Dr. R. Paulin from Saclay and the Nb sample was prepared by P. Bujard of our department.

Stimulating discussions of the results and their analysis were had with members of the calculation group of Prof. M. Peter. Dr. W. Andreoni-Kay, Dr. M. Dacorogna and Dr. T. Jarlborg have communicated to us band structure calculation for Nb.

This work was supported by the Swiss National Science Foundation.

REFERENCES

[1] R. N. WEST, Adv. in Phys. *22*, 263 (1973).
[2] P. HAUTOJARVI (ed.): *Positrons in solids, Topics in current physics*, vol. 12 (Springer, 1979).
[3] J. P. CARBOTTE and S. KAHANA, Phys. Rev. *139*, A213 (1965).
[4] S. BERKO, M. HAGHOOIE and J. J. MADER, Phys. Lett. 63A, 335 (1977).
[5] R. N. WEST, J. MAYERS and P. A. WALTERS, J. Phys. E: Sci. Instrum. *14*, 478 (1981).
[6] A. A. MANUEL, S. SAMOILOV, Ø. FISCHER, M. PETER and A. P. JEAVONS, Helv. Phys. Acta *52*, 255 (1979).
[7] A. P. JEAVONS, Nucl. Inst. and Meth. *156*, 41 (1978).
[8] A. A. MANUEL, Ph.D. No 1889, Geneva University, Switzerland, 1978.
[9] A. P. JEAVONS, G. CHARPAK and R. J. STUBBS, Nucl. Inst. and Meth. *124*, 491 (1975); A. P. JEAVONS and C. CATE, IEEE Trans. Nucl. Sc. *23*, 640 (1976).
[10] G. CHARPAK, R. BOUCLIER, T. BRESSANI, J. FAVIER and C. ZUPANCIC, Nucl. Inst. and Meth. *62*, 262 (1968).
[11] E. GATTI, A. LONGONI, H. OKUNO and P. SEMENZA, Nucl. Inst. and Meth. *163*, 83 (1979).
[12] D. CHU, K. C. TAM, V. PEREZ-MENDEZ, C. B. LIM, D. LAMBERT and S. N. KAPLAN, IEEE Trans. Nucl. Sc. *23*, 634 (1976).
[13] S. BRANDT, C. GRUPEN, M. ROSCHANGAR, B. SCHOFER and G. KNIES, Nucl. Inst. and Meth. *145*, 593 (1977).
[14] F. SAULI, Nucl. Inst. and Meth. *156*, 147 (1978).
[15] N. SHIOTANI, T. OKADA, T. MIZOGUCHI and H. SEZIKAWA, J. Phys. Soc. Jap. *38/2*, 423 (1975).
[16] S. WAKOH, Y. KUBO and J. YAMASHITA, J. Phys. Soc. Jap. *38/2*, 416 (1975).
[17] A. A. MANUEL, *13th Polish Seminar on Positron Annihilation, Piechowice*, April 21–26, 1980, paper 19 (abstract only).
[18] R. N. WEST, *Physics on Transition Metals 1980*, Leeds (UK), August 18–22, 1980, Inst. Phys. Conf. No 55 chapter 1 p. 35.
[19] P. BUJARD, R. SAJINES, E. WALKER, J. ASKENAZI and M. PETER, J. Phys. F: Metal Phys. *11*, 775 (1981).
[20] A. A. MANUEL: Seminar given at the Enrico Fermi School "Positrons in solids", July 1981, to be published.
[21] W. ANDREONI-KAY and T. JARLBORG: private communication.
[22] D. G. LOCK, V. H. C. CRISP and R. N. WEST, J. Phys. F: Metal Phys. *3*, 561 (1973).